

1 **Technical note: 12-km resolution capability for the global GEOS-Chem model of atmospheric** 2 **composition**

3 Xiaolin Wang¹, Melissa P. Sulprizio¹, Yuyao Zhuge², Randall V. Martin², Daniel J. Jacob¹

4 ¹ School of Engineering and Applied Sciences, Harvard University, Cambridge, MA, USA

5 ² Department of Energy, Environmental & Chemical Engineering, Washington University in St.
6 Louis, St. Louis, MO, USA

7

8 *Correspondence to:* Xiaolin Wang (wangxi@g.harvard.edu)

9

10

11 **Abstract**

12

13 We present a new 12-km nested resolution capability in the GEOS-Chem global model of
14 atmospheric composition. This capability can be applied to simulations for any user-selected
15 domain worldwide from March 2021 onward by accessing a new hourly cubed-sphere C720
16 (~~$\approx 0.125^\circ \times 0.15625^\circ$~~ (approximately 12 km \times 12 km² km resolution)) global wind archive from
17 the NASA GEOS-FP meteorological data assimilation system. We regrided the archive to
18 support rectilinear GEOS-Chem Classic nested grid simulations worldwide at $0.125^\circ \times 0.15625^\circ$
19 resolution and denote this as the 12-km GEOS-Chem capability. We evaluate this 12-km
20 configuration of GEOS-Chem by comparison with the standard 25-km ($0.25^\circ \times 0.3125^\circ$
21 resolution) nested configuration in simulations of transport tracers, oxidant-aerosol chemistry,
22 and inversions of satellite data using the Integrated Methane Inversion (IMI). The 12-km
23 simulation features stronger vertical transport (up to 20% lower surface ²²²Rn concentrations)
24 because it better captures ~~eddy fluxes~~ horizontal convergence both spatially and temporally.
25 Aerosol lifetimes against deposition ~~and stratosphere-troposphere exchange~~ are similar at the
26 ~~two resolutions~~ shorter by a few percent. The 12-km oxidant-aerosol chemistry can better
27 simulate urban observations of NO₂, ~~with~~ and shows stronger ozone urban titration ~~but~~ together
28 with slightly higher surface ozone background due to enhanced vertical transport. 12-km and 25-
29 km inversions using the IMI show highly consistent results on the regional scale, but the 12-km
30 inversion provides greater information and improved spatial detail to resolve emissions from
31 different sectors.

32

33 **1. Introduction**

34 GEOS-Chem (<http://geos-chem.org>) is an open-source global 3-D model of atmospheric
35 chemistry originally described by Bey et al. (2001) and used by hundreds of research groups
36 around the world for a wide range of applications. ~~#~~ The standard offline configuration of GEOS-
37 Chem is driven by archived Goddard Earth Observing System (GEOS) meteorological data from
38 the NASA Global Modeling and Assimilation Office (GMAO), with no feedback of chemistry

39 [on meteorology](#). GEOS-Chem can also operate online in dynamical coupling with Earth system
40 [models \(Fritz et al., 2022; Hu et al., 2018; Lu et al., 2020\) or the WRF regional model \(Lin et al.,](#)
41 [2020\)](#). Here we introduce the capability to conduct [offline](#) GEOS-Chem simulations at $0.125^\circ \times$
42 0.15625° ($\approx 12 \text{ km} \times 12 \text{ km}$) resolution by exploiting a new GEOS advection data archive
43 [combined with the nested capability of GEOS-Chem \(grid-scale winds\) available from March](#)
44 [2021 onward](#). This enables low-cost, reproducible, high-resolution simulations of atmospheric
45 chemistry and air quality anywhere in the world [and for any period from March 2021](#)
46 [onward through the nested capability of GEOS-Chem](#). In what follows we ~~will~~ refer to it as the
47 12-km capability in GEOS-Chem.

48 The open-access GEOS global meteorological datasets used to drive GEOS-Chem are produced
49 at GMAO by data assimilation on the cubed-sphere grid of the underlying GEOS Earth system
50 model (ESM) and then archived on a rectilinear latitude-longitude grid for public dissemination.
51 The GEOS-Chem Support Team extracts from these archives the data needed to run GEOS-
52 Chem and distributes them to users as an open dataset library through the Amazon Web Services
53 (AWS) cloud (Zhuang et al., 2019; Martin et al., 2022). GEOS-Chem users may choose from
54 three main datasets: the Modern-Era Retrospective Analysis for Research and Applications,
55 version 2 (MERRA-2; 1980-present) at $0.5^\circ \times 0.625^\circ$ resolution, the GEOS Forward Processing
56 (GEOS-FP; 2014-present) at $0.25^\circ \times 0.3125^\circ$ resolution, and the GEOS for Instrument Teams
57 (GEOS-IT; 1998-present) at $0.5^\circ \times 0.625^\circ$ ~~resolution~~ or native cubed-sphere C180 resolution (180
58 grid cells per cubed-sphere side, [corresponding to \$\approx 0.5^\circ \times 0.625^\circ\$ approximately \$50 \text{ km} \times 50 \text{ km}\$](#)
59 resolution). MERRA-2 provides a long stable record with fixed physics and data assimilation
60 algorithms, GEOS-IT is the next-generation stable record with updated physics and data
61 assimilation, and GEOS-FP is the operational product generated in near real time using the latest
62 validated GEOS system. GEOS-FP operates at native C720 resolution (\approx
63 [\$0.125^\circ \times 0.15625^\circ\$ \(approximately \$12 \text{ km} \times 12 \text{ km}\$ \)](#) but the data archive was previously made
64 available only at $0.25^\circ \times 0.3125^\circ$ resolution. Since March 2021, GMAO has been producing a
65 native-resolution hourly C720 GEOS-FP advection archive specifically to serve GEOS-Chem
66 needs, and this is what we use to enable the 12-km capability in GEOS-Chem.

67 GEOS-Chem operates in two modes, Classic (GC-Classic) and High-Performance (GCHP)
68 (Martin et al., 2022). GC-Classic is designed for easy use on the rectilinear longitude-latitude
69 grid and operates on single-node mode with shared-memory parallelization. GCHP enables high-
70 resolution simulations using distributed-memory parallelization (MPI) on the cubed-sphere [grid](#)
71 with efficient multi-node scalability extending to thousands of cores (Eastham et al., 2018). Both
72 GC-Classic and GCHP can ~~operate on~~ [use the native original rectilinear GEOS \[grid archive\]\(#\)](#)
73 [available at resolutions ~~but~~ down to \$0.25^\circ \times 0.3125^\circ\$, with GCHP converting these inputs to its](#)
74 [cubed-sphere grid at runtime. They can](#) also [operate](#) at coarser resolutions for computational
75 economy using regridded GEOS data archived on AWS as part of the GEOS-Chem input dataset
76 library. Global GC-Classic simulations thus typically use $2^\circ \times 2.5^\circ$ or $4^\circ \times 5^\circ$ GEOS data. GC-

77 Classic includes a one-way nested capability to conduct ~~native-resolution~~regional simulations
78 over limited domains with archived dynamic boundary conditions from a coarse-resolution
79 simulation (Wang et al., 2004). GCHP includes a stretched-grid capability to enable higher-
80 resolution two-way nesting over target regions (Bindle et al., 2021). Emission and surface type
81 information are generally available at $0.1^\circ \times 0.1^\circ$ (~~≈ 10 -km~~) resolution from the GEOS-Chem
82 input dataset library, from which they are regridded on the fly within GEOS-Chem at the desired
83 resolution using the HEMCO software tool (Lin et al., 2021). The one-way nested GC-Classic
84 capability at GEOS-FP $0.25^\circ \times 0.3125^\circ$ (~~\approx~~ referred to as 25-km) resolution is widely used for air
85 quality applications (Kim et al., 2015; Zhang et al., 2015) and for inversions of greenhouse gas
86 data to infer surface fluxes (Varon et al., 2022).

87 Here, we implement the GEOS-FP native C720 advection archive for use in GC-Classic nested-
88 grid simulations. This 12-km capability can be applied over any user-selected domain
89 worldwide, and for any period from March 2021 onward. It has been released in GEOS-Chem
90 ~~version~~ 14.6.0 (<https://doi.org/10.5281/zenodo.15243271>). We describe the 12-km capability in
91 Section 2 and compare its transport to the standard 25-km nested GC-Classic configuration in
92 Section 3. We then demonstrate its application to a full-chemistry simulation over the North
93 China Plain (Section 4) and to the inversion of satellite observations using the Integrated
94 Methane Inversion (IMI) framework (Section 5).

95 2. GEOS-Chem simulation at 12-km resolution

96 GC-Classic allows users to conduct nested simulations over any domain of interest using the
97 GEOS meteorological archives as input and with rectilinear coordinates specified at runtime.
98 This framework was first introduced by Wang et al. (2004) and updated to $0.25^\circ \times 0.3125^\circ$
99 resolution by Zhang et al. (2015) and Kim et al. (2015). The nested simulations are conducted as
100 a regional model with boundary conditions provided by a separate global simulation at $2^\circ \times 2.5^\circ$
101 or $4^\circ \times 5^\circ$ resolution that provides dynamic chemical fields updated every three hours.

102 Here we use the new global C720 GEOS-FP hourly advection archive, regridded to $0.125^\circ \times$
103 0.15625° , to ~~enable~~produce the 12-km advection archive that enables GC-Classic nested-grid
104 simulations at ~~12-km~~ $0.125^\circ \times 0.15625^\circ$ resolution. The 12-km advection archive includes
105 horizontal wind vectors, surface pressure, and specific humidity on 72 vertical levels extending
106 from the surface to 0.01 hPa (model top). Horizontal wind vectors are converted from cubed-
107 sphere C720 mass flux data for use in the GC-Classic transport scheme (Lin and Rood, 1996).
108 Surface pressure is needed to infer the vertical air mass fluxes from the horizontal air mass fluxes
109 by mass conservation. Specific humidity is needed to convert wet air fluxes and pressure in the
110 GEOS data to dry air fluxes and pressures used in GEOS-Chem. The regridding from cubed-
111 sphere C720 to the rectilinear $0.125^\circ \times 0.15625^\circ$ grid yields an approximately 12 km \times 12 km
112 horizontal scale over midlatitudes, slightly coarser toward the equator and finer toward the poles.

113 Table 1 summarizes the GEOS-FP input data for the 12-km configuration as compared to the 25-
 114 km configuration. The idea behind the advection archive is that higher resolution is most needed
 115 for the winds to better represent eddy flows and to leverage the $0.1^\circ \times 0.1^\circ$ resolution of the
 116 emission data. Limiting the number of variables in the advection archive enables global [data](#)
 117 [storage at C720](#). ~~The 12-km advection archive has hourly temporal resolution, compared to 3-~~
 118 ~~hourly resolution for the 3-D variables in the 25-km archive.~~ [computational storage at C720](#).
 119 Other non-advection meteorological inputs including convective mass fluxes and vertical mixing
 120 depths are from the standard GEOS-FP archive at $0.25^\circ \times 0.3125^\circ$ resolution and are dynamically
 121 regridded to $0.125^\circ \times 0.15625^\circ$ [on the fly during the 12-km simulation at runtime](#). Most emission
 122 datasets are available on a $0.1^\circ \times 0.1^\circ$ grid and are regridded [on the fly at runtime](#) to the simulation
 123 resolution using HEMCO (Lin et al., 2021). The 12-km [advection archive](#) ~~includes horizontal~~
 124 ~~wind vectors, surface pressure, and specific humidity on 72 vertical levels extending from the~~
 125 ~~surface to 0.01 hPa (model top). Surface pressure is needed to infer the vertical air mass fluxes~~
 126 ~~from the horizontal air mass fluxes by mass conservation. Specific humidity is needed to convert~~
 127 ~~wet air fluxes and pressure in the GEOS data to dry air fluxes and pressures used in GEOS-~~
 128 ~~Chem.~~ [available globally](#). ~~The 12-km advection archive has hourly temporal resolution, compared~~
 129 ~~to 3-hourly resolution for the 3-D variables in the 25-km archive.~~ We [also](#) maintain separate 12-
 130 km advection archives for five continental regions (Africa, Asia, Europe, North America, and
 131 South America) to reduce data size and thereby speed up data access and processing over the
 132 user-selected nested domains (<https://registry.opendata.aws/geoschem-nested-input-data/>); [latest](#)
 133 [access: 21 October 2025](#)).

134 All simulations presented here were carried out on the Harvard Cannon v2.0 supercomputing
 135 cluster using compute nodes equipped with dual-socket Intel Xeon Platinum 8480CL CPUs (56
 136 cores each, base frequency ~ 2.9 GHz). Each simulation used 48 physical CPU cores and ran on a
 137 single node. We find that the 12-km simulation wall-time is about $7 \times$ [times](#) that of a 25-km
 138 simulation over the same domain. This is driven by the $4 \times$ [times](#) increase in grid cells and the $2 \times$
 139 [times](#) reduction in timestep. The 1-month full-chemistry simulation presented in Section 4 took
 140 26 wall-time hours to complete at 12-km resolution.

141

142 **Table 1.** GEOS-FP meteorological data archives available for driving GEOS-~~Chem~~[Chem](#) at
 143 [0.125°×0.15625° \(12-km\) and 0.25°×0.3125° \(25-km\) resolutions](#)^a.

GEOS-Chem simulation	12×12 km²-km	25×25 km²-km
Archive period	March 2021-present	January 2014-present
Horizontal resolution (advection)	$0.125^\circ \times 0.15625^\circ$	$0.25^\circ \times 0.3125^\circ$
Temporal resolution (advection)	Hourly	3-hourly

Horizontal resolution (other)	0.25°×0.3125° regrided to 0.125°×0.15625°	0.25°×0.3125°
Temporal resolution (other)	3-hourly or hourly ^b	3-hourly or hourly
Timestep ^c	Transport 150 s Non-transport 300 s	Transport 300 s Non-transport 600 s

- 144 a. For GC-Classic simulations at 0.125°×0.15625° and 0.25°×0.3125° resolutions (~~≈12×12~~
145 ~~km² and 25×25 km²~~) with 72 hybrid sigma-pressure vertical levels extending up to 0.01
146 hPa. GEOS-FP meteorological data used as GEOS-Chem input include advection
147 variables (horizontal wind vectors, surface pressure, specific humidity) and other
148 variables driving convective transport, planetary boundary layer (PBL) mixing,
149 emissions, radiation, chemistry, and deposition. The full list of variables is at:
150 https://wiki.seas.harvard.edu/geos-chem/index.php/List_of_GEOS-FP_met_fields. The
151 advection variables are grouped in a separate advection archive for 12-km applications.
152 The 12-km and 25-km archives are available globally, and also for individual continents
153 to speed up data extraction.
- 154 b. Hourly for two-dimensional fields such as surface properties and PBL depth; 3-hourly for
155 three-dimensional fields such as temperature and convective mass flux.
- 156 c. Recommended timesteps for operator splitting (Philip et al., 2016), can be adjusted by
157 user. Non-transport operators include emissions, chemistry, and deposition.

158

159 3. Transport tracer simulations

160 We use the TransportTracers simulation of GEOS-Chem ([https://wiki.seas.harvard.edu/geos-](https://wiki.seas.harvard.edu/geos-chem/index.php/TransportTracers_simulation)
161 [chem/index.php/TransportTracers_simulation](https://wiki.seas.harvard.edu/geos-chem/index.php/TransportTracers_simulation) Zhang et al., 2021) to evaluate model transport and
162 scavenging processes. This simulation includes 21 generic species (tracers) to test the different
163 components of GEOS-Chem transport. We focus here on the radionuclide tracers radon-222
164 (²²²Rn), lead-210 (²¹⁰Pb), and beryllium-7 (⁷Be), which are routinely used to benchmark transport
165 and wet deposition in GEOS-Chem (Liu et al., 2001; Yu et al., 2018). [These tracers are](#)
166 [particularly useful for evaluating model vertical transport, whereas grid-scale vertical winds are](#)
167 [calculated from horizontal mass flux convergence and is not directly available in the model.](#) The
168 nested-grid simulations are conducted over eastern China (100–125°E, 17–45°N, domain shown
169 in Figure 1) at both 0.125°×0.15625° and 0.25°×0.3125 resolutions for February and June 2022.
170 Initial conditions are generated from spin-up simulations at the same resolutions, starting from
171 October 2021 (corresponding to spin-up periods of 4 months for February and 8 months for
172 June). The boundary conditions are updated every three hours from a global simulation at 2° ×
173 2.5° resolution.

174 Figure 1 shows surface ^{222}Rn concentrations from the 12-km simulation and relative differences
175 with the 25-km simulation. ^{222}Rn in the simulation has a spatially uniform soil source and is
176 removed by radioactive decay with a half-life of 3.8 days, making it a sensitive tracer for vertical
177 transport in the troposphere (Liu et al., 2001; Yu et al., 2018). Surface ^{222}Rn concentrations are
178 lower by 0–20% at 12-km than at 25-km resolution. Differences are most pronounced over
179 complex terrain such as Sichuan and Taiwan. The total ^{222}Rn burden in the two simulations is the
180 same, and the difference is in the vertical distribution (FigureFigures 2 and 3). The 12-km
181 simulation shows ~~reduced~~lower ^{222}Rn concentrations in the lower troposphere and
182 ~~enhanced~~higher concentrations in the middle-to-upper troposphere, indicating stronger vertical
183 transport. ~~Differences~~The lower ^{222}Rn concentrations in the tropical stratosphere in June,
184 combined with the lower ^7Be concentrations below the tropopause, may reflect greater restriction
185 of transport across the tropopause at higher resolution (Stanevich et al., 2020) but would require
186 further investigation because the absolute changes are most pronounced over complex terrain
187 such as Sichuan and Taiwanvery small.

188 Transport processes in GEOS-Chem include grid-resolved advection (winds), sub-grid
189 parameterized convection (convective mass fluxes), and PBL-mixing (Lin and McElroy, 2010).
190 ~~We find that the differences between the 12-km and 25-km simulations persist even when~~
191 ~~convection and PBL mixing (both from the 25-km archive) are shut off. The enhanced vertical~~
192 ~~transport at 12-km is thus driven by the improved resolution of advection, both spatially and~~
193 ~~temporally (1-hour versus 3-hour). When winds are averaged in space and time relative to the~~
194 ~~parent GEOS ESM simulation (here at C720 with 7.5-minute timesteps), vertical eddy fluxes are~~
195 ~~lost. This has been recognized previously as a major driver of differences between GEOS-Chem~~
196 ~~simulations at different resolutions (Yu et al., 2018). The 12-km simulation has no spatial~~
197 ~~averaging of winds relative to the parent GEOS ESM and only 1-hour temporal averaging, and~~
198 ~~therefore retains more of the native GEOS ESM vertical motions to produce stronger vertical~~
199 ~~eddy fluxes of ^{222}Rn .~~Differences between the 12-km and 25-km simulations could reflect
200 stronger vertical winds at 12-km due to better resolved horizontal convergence (Yu et al., 2018)
201 and better resolution of concentration gradients leading to stronger tracer convergence for the
202 same winds. To separate these two effects, we conducted a 12-km sensitivity simulation driven
203 by the 3-hourly 25-km advection archive regridded to 12-km resolution during runtime (right
204 columns of Figures 1-3). We find that both effects contribute.

205 ^{210}Pb (half-life of 22.3 years) is produced by the decay of ^{222}Rn , and ^7Be (half-life of 53.3 days)
206 is generated by cosmic-ray interactions with atmospheric oxygen and nitrogen at high altitudes.
207 Both radionuclides rapidly attach to aerosol particles and are subsequently transported and
208 removed by wet and dry deposition. This makes ^{210}Pb useful to evaluate aerosol transport and
209 removal processes, with ^7Be providing complementary information on stratosphere–troposphere
210 exchange and tropospheric subsidence (Liu et al., 2001). Comparisons of 12-km and 25-km
211 simulations for ^{210}Pb show similar differences as for ^{222}Rn (FigureFigures 2 and 3) but weaker in
212 magnitude because the ^{210}Pb source is more diffuse. Lifetimes against deposition differ by less

213 than 2% between the 12-km and 25-km simulations. Comparisons for ^7Be also show weaker
214 differences than for ^{222}Rn because vertical transport of ^7Be in the troposphere is mainly by large-
215 scale subsidence, which is less sensitive to eddy motions. ~~We find no significant difference in~~
216 ~~transport of ^7Be across the tropopause. The ^7Be lifetime against deposition is 3% higher at 25-km~~
217 ~~resolution, explaining the slightly higher overall tropospheric concentrations.~~

218

219 4. Full-chemistry simulations

220 We perform 1-month full-chemistry simulations for February and June of 2022 over the North
221 China Plain (NCP; domain shown in Figure 34) at 12-km and 25-km horizontal resolutions for
222 comparison. The full-chemistry configuration of GEOS-Chem includes detailed ozone- NO_x -
223 VOCs-aerosol-halogen tropospheric and stratospheric chemistry (Wang et al., 2021). Boundary
224 conditions are provided by a global $2^\circ \times 2.5^\circ$ GEOS-Chem simulation and updated every three
225 hours, and spin-up simulations are conducted from October 2021 to generate initial conditions.
226 Monthly anthropogenic emissions are from the MIXv2 Asian emission inventory at $0.1^\circ \times 0.1^\circ$
227 resolution for 2017, scaled to 2022 using province-level emission data from the MEIC v1.4
228 inventory (Zheng et al., 2018) and mapped to the 12-km and 25-km grids using HEMCO. We
229 compare the model simulations of surface NO_2 , ozone, and fine particulate matter ($\text{PM}_{2.5}$)
230 concentrations to hourly observations from 361 sites operated by the China National
231 Environmental Monitoring Centre (CNEMC; <http://www.cnemc.cn>, last assess: 23 May 2023).
232 The sites are mainly urban. We remove anomalous observations at each site following the quality
233 control protocols described in Lu et al. (2018). We sample model outputs at the observation sites
234 for comparisons.

235 Figure 34 shows the afternoon (13-18 local time) surface NO_2 concentrations over the NCP in
236 June 2022 and the effect of model resolution. The finer structure at 12-km resolution is evident
237 and largely reflects the ability to exploit the higher resolution of emissions. Comparison to
238 CNEMC observations (Figure 4a5a) shows a low bias in the model, likely reflecting the near-
239 source locations of the sites, but the bias is reduced at 12-km resolution. The 12-km simulation
240 does not improve the correlation with observations for individual CNEMC sites, which could
241 reflect errors in model transport or in the spatial distribution of emissions.

242 Figure 56 compares simulated maximum daily 8-h average (MDA8) surface ozone
243 concentrations at 12-km and 25-km resolutions in June 2022. The differences between the two
244 resolutions are generally smaller than 5 ppb, and there is no significant difference in the fit to
245 observations (Figure 4b5b). Background ozone concentrations increase by up to 3 ppb over the
246 northern NCP region, likely driven by increased vertical transport of ozone from aloft as seen in
247 the simulated ^7Be concentrations in Figure 1. Increasing the model resolution to 12-km decreases
248 surface ozone concentrations by about 3 ppb in Beijing and 6 ppb in Tianjin city core areas, as
249 expected from higher NO_x concentrations driving stronger ozone titration, whereas suburban

250 areas exhibit ozone increases of no more than 2 ppb. These effects are too small to be effectively
251 evaluated in the comparison to observations (Figure [4b5b](#)).

252 ~~Figures 6~~[Figure 7](#) shows the daily-averaged total PM_{2.5} mass concentrations in February 2022,
253 where PM_{2.5} is computed in the model as the sum of fine aerosol components (Zhai et al., 2021).
254 We focus on February here because PM_{2.5} concentrations are higher in winter than in summer
255 (Zhai et al., 2019). PM_{2.5} concentrations are in general slightly lower at 12-km resolution
256 because of the enhanced vertical transport. However, higher concentrations are found in a few
257 urban hotspots due to primary organic aerosol emissions from combustion that are better
258 resolved [spatially](#). Again, differences are too small to be arbitrated by the observations (Figure
259 [4e5c](#)).

261 5. Application to the Integrated Methane Inversion (IMI)

262 The IMI applies the nested GEOS-Chem as forward model in regional analytical inversions of
263 TROPOMI satellite observations of methane columns to optimize methane emissions (Estrada et
264 al., 2025; Varon et al., 2022). [It uses Bayesian inference to minimize the mismatch between the
265 TROPOMI methane column observations and the corresponding concentrations simulated by
266 GEOS-Chem, regularized by prior information on emissions. GEOS-Chem is applied to
267 construct the Jacobian matrix describing the sensitivity of TROPOMI observations to emissions
268 as simulated by the model transport. This is then used together with the TROPOMI observations,
269 prior emission estimates, and prior and observational error statistics to derive optimized
270 \(posterior\) emissions.](#) The TROPOMI satellite observations are at 5.5×7 km² pixel resolution so
271 there is potential benefit for conducting the inversion at 12-km resolution using our new GEOS-
272 Chem capability. The 12-km IMI configuration was previously applied in Wang et al.
273 ~~(2025)~~[\(2026\)](#) to quantify methane emissions across 12 U.S. urban areas. Here we examine how
274 inversion results vary between 12-km and 25-km resolution, focusing on the Houston urban area
275 in eastern Texas as an example.

276 The IMI inversion procedure is described by Estrada et al. (2025) and Hancock et al. (2025),
277 including the design of state vector, error estimates, and optimization strategy. Here we optimize
278 annual methane emissions in 2022 over a 3°×4° (latitude×longitude) domain encompassing
279 Houston and its surrounding area as shown in Figure [78](#). The state vector to be optimized
280 consists of emissions in each land-containing grid cell of the 3°×4° domain (496 elements at 12-
281 km resolution and 164 elements at 25-km resolution) and boundary conditions on each lateral
282 edge (4 elements). Our prior estimates of anthropogenic emissions are from the U.S.
283 Environmental Protection Agency Greenhouse Gas Inventory (GHGI) at 0.1°×0.1° resolution for
284 2020 (Maasackers et al., 2023). Natural emissions follow the default configuration as described
285 in Estrada et al. (2025). We assume a lognormal prior error probability density function (PDF)
286 for emissions with a geometric error standard deviation of 2.0 (Bruno et al., 2025), and a normal

287 error PDF for boundary conditions with a 10 ppb error standard deviation. The IMI analytical
288 inversion returns ~~optimized~~ (posterior) emissions and a posterior error covariance matrix from
289 which the averaging kernel matrix can be derived as a measure of information content from the
290 observations (Brasseur and Jacob, 2017).

291 The prior estimate of total emissions over the $3^{\circ} \times 4^{\circ}$ inversion domain is 790 Gg a^{-1} (Figure 78).
292 Total posterior emissions are 50% higher than the prior estimate and agree closely between the
293 12-km inversion (1260 Gg a^{-1}) and the 25-km inversion (1170 Gg a^{-1}). The 12-km inversion
294 results, when averaged over the 25-km grid, show a high degree of consistency with the 25-km
295 inversion results over the inversion domain (spatial correlation coefficient = 0.92). The trace of
296 the averaging kernel matrix defines the Degrees of Information for Signal (DOFS) indicating the
297 number of pieces of information that can be obtained from the observations through the inversion
298 independently from the prior estimate. The DOFS for the $3^{\circ} \times 4^{\circ}$ domain is 24.4 for the 12-km
299 inversion, higher than the 16.8 for the 25-km inversion. Conducting the inversion at higher
300 resolution allows for more information on emissions to be extracted from the observations.

301 Another advantage of the higher-resolution inversion is better separation of the sectors
302 contributing to methane emissions. Sectoral information in the inversion is obtained by
303 attributing the posterior/prior emission ratios for each grid cell to the different sectors
304 contributing emissions to that grid cell in the prior estimate (Wecht et al., 2014). Higher spatial
305 resolution in the inversion reduces spatial overlap between sectors.

306 6. In summary, Conclusion

307 We have implemented a 12-km resolution nested capability in the GEOS-Chem global model of
308 atmospheric chemistry by taking advantage of a new hourly GEOS advection archive available
309 globally from March 2021 onward and freely distributed to GEOS-Chem users through the AWS
310 cloud. We compared the 12-km simulation to the standard 25-km nested simulation in GEOS-
311 Chem for transport tracers (^{222}Rn , ^{210}Pb , ^7Be), ozone-aerosol chemistry, and inversion of methane
312 satellite data where GEOS-Chem provides the forward model. The 12-km simulation has
313 stronger vertical transport (up to 20% decrease in ^{222}Rn surface concentrations) because of
314 improved representation of ~~eddy fluxes~~ horizontal convergence. It shows finer spatial structure in
315 surface pollutants (NO_2), with improved capability to reproduce urban observations. It better
316 represents surface ozone titration in urban air and slightly increases the surface ozone
317 background by increasing vertical transport. Application to the Integrated Methane Inversion
318 (IMI) shows regional-scale results consistent with a 25-km inversion but higher information
319 content and greater spatial detail. Overall, this 12-km capability further extends the application
320 of GEOS-Chem in regional atmospheric chemistry and in the use of high-resolution satellite
321 observations to quantify emissions of air pollutants and greenhouse gases at fine spatial scales.
322 Higher model resolution improves the representation of finer concentration gradients and inverse
323 model sensitivity through improved transport and chemistry.

324

325 **Code and data availability.**

326 The source code of GEOS-Chem ~~version~~ 14.6.0 is publicly available at
327 <https://doi.org/10.5281/zenodo.15243271>. The GEOS-FP meteorological fields used to drive
328 GEOS-Chem are available on the Amazon Web Services (AWS) cloud
329 (<https://s3.amazonaws.com/gcgrid/index.html>; last access: ~~28~~²¹ October ~~2024~~²⁰²⁵).

330

331 **Author contributions.**

332 XW and DJJ conceptualized the research. XW performed the analyses and data visualization.
333 XW and MPS developed the model code. MPS, YZ and RVM contributed to the data collection.
334 XW and DJJ wrote the manuscript with input from all authors.

335

336 **Competing interests.**

337 The authors declare no competing interests.

338

339 **Financial support.** This research has been supported by the United Nations Environment
340 Programme's International Methane Emissions Observatory (IMEO) and by the NASA
341 Atmospheric Composition Modeling and Analysis Program (grant no. 80NSSC23K0926). RVM
342 acknowledges support from the U.S. National Science Foundation (NSF; grant no. 2244984).

343

344 **References**

345 ~~Bruno, J. H., Jacob, D. J., Wang, X., Sulprizio, M. P., Estrada, L. A., Varon, D. V., Wofsy, S. C.,~~
346 ~~Omara, M., and Gautam, R.: Integrating MethaneAIR aircraft and TROPOMI satellite~~
347 ~~observations in the Integrated Methane Inversion (IMI) to optimize methane emissions,~~
348 ~~submitted, 2025.~~

349 Bey, I., Jacob, D. J., Yantosca, R. M., Logan, J. A., Field, B. D., Fiore, A. M., Li, Q., Liu, H. Y.,
350 Mickley, L. J., and Schultz, M. G.: Global modeling of tropospheric chemistry with assimilated
351 meteorology: Model description and evaluation, *J. Geophys. Res. Atmospheres*, 106, 23073–
352 23095, <https://doi.org/10.1029/2001JD000807>, 2001.

353 Bindle, L., Martin, R. V., Cooper, M. J., Lundgren, E. W., Eastham, S. D., Auer, B. M., Clune, T.
354 L., Weng, H., Lin, J., Murray, L. T., Meng, J., Keller, C. A., Putman, W. M., Pawson, S., and
355 Jacob, D. J.: Grid-stretching capability for the GEOS-Chem 13.0.0 atmospheric chemistry
356 model, *Geosci. Model Dev.*, 14, 5977–5997, <https://doi.org/10.5194/gmd-14-5977-2021>, 2021.

- 357 Brasseur, G. P. and Jacob, D. J.: Modeling of Atmospheric Chemistry, 1st ed., Cambridge
358 University Press, <https://doi.org/10.1017/9781316544754>, 2017.
- 359 [Bruno, J. H., Jacob, D. J., Wang, X., Sulprizio, M. P., Estrada, L. A., Varon, D. J., Wofsy, S. C.,
360 Omara, M., and Gautam, R.: Integrating MethaneAIR aircraft and TROPOMI satellite
361 observations in the Integrated Methane Inversion \(IMI\) to optimize methane emissions,
362 EGU sphere, 1–23, <https://doi.org/10.5194/egusphere-2025-4626>, 2025.](#)
- 363 Eastham, S. D., Long, M. S., Keller, C. A., Lundgren, E., Yantosca, R. M., Zhuang, J., Li, C.,
364 Lee, C. J., Yannetti, M., Auer, B. M., Clune, T. L., Kouatchou, J., Putman, W. M., Thompson, M.
365 A., Trayanov, A. L., Molod, A. M., Martin, R. V., and Jacob, D. J.: GEOS-Chem High
366 Performance (GCHP v11-02c): a next-generation implementation of the GEOS-Chem chemical
367 transport model for massively parallel applications, *Geosci. Model Dev.*, 11, 2941–2953,
368 <https://doi.org/10.5194/gmd-11-2941-2018>, 2018.
- 369 Estrada, L. A., Varon, D. J., Sulprizio, M., Nesser, H., Chen, Z., Balasus, N., Hancock, S. E., He,
370 M., East, J. D., Mooring, T. A., Oort Alonso, A., Maasackers, J. D., Aben, I., Baray, S., Bowman,
371 K. W., Worden, J. R., Cardoso-Saldaña, F. J., Reidy, E., and Jacob, D. J.: Integrated Methane
372 Inversion (IMI) 2.0: an improved research and stakeholder tool for monitoring total methane
373 emissions with high resolution worldwide using TROPOMI satellite observations, *Geosci. Model
374 Dev.*, 18, 3311–3330, <https://doi.org/10.5194/gmd-18-3311-2025>, 2025.
- 375 [Fritz, T. M., Eastham, S. D., Emmons, L. K., Lin, H., Lundgren, E. W., Goldhaber, S., Barrett, S.
376 R. H., and Jacob, D. J.: Implementation and evaluation of the GEOS-Chem chemistry module
377 version 13.1.2 within the Community Earth System Model v2.1, *Geosci. Model Dev.*, 15, 8669–
378 8704, <https://doi.org/10.5194/gmd-15-8669-2022>, 2022.](#)
- 379 Hancock, S. E., Jacob, D. J., Chen, Z., Nesser, H., Davitt, A., Varon, D. J., Sulprizio, M. P.,
380 Balasus, N., Estrada, L. A., Cazorla, M., Dawidowski, L., Diez, S., East, J. D., Penn, E., Randles,
381 C. A., Worden, J., Aben, I., Parker, R. J., and Maasackers, J. D.: Satellite quantification of
382 methane emissions from South American countries: a high-resolution inversion of TROPOMI
383 and GOSAT observations, *Atmospheric Chem. Phys.*, 25, 797–817, [https://doi.org/10.5194/acp-
384 25-797-2025](https://doi.org/10.5194/acp-25-797-2025), 2025.
- 385 [Hu, L., Keller, C. A., Long, M. S., Sherwen, T., Auer, B., Da Silva, A., Nielsen, J. E., Pawson, S.,
386 Thompson, M. A., Trayanov, A. L., Travis, K. R., Grange, S. K., Evans, M. J., and Jacob, D. J.:
387 Global simulation of tropospheric chemistry at 12.5km resolution: performance and evaluation of
388 the GEOS-Chem chemical module \(v10-1\) within the NASA GEOS Earth system model \(GEOS-
389 5 ESM\), *Geosci. Model Dev.*, 11, 4603–4620, <https://doi.org/10.5194/gmd-11-4603-2018>, 2018.](#)
- 390 Kim, P. S., Jacob, D. J., Fisher, J. A., Travis, K., Yu, K., Zhu, L., Yantosca, R. M., Sulprizio, M.
391 P., Jimenez, J. L., Campuzano-Jost, P., Froyd, K. D., Liao, J., Hair, J. W., Fenn, M. A., Butler, C.
392 F., Wagner, N. L., Gordon, T. D., Welti, A., Wennberg, P. O., Crounse, J. D., St. Clair, J. M.,
393 Teng, A. P., Millet, D. B., Schwarz, J. P., Markovic, M. Z., and Perring, A. E.: Sources,
394 seasonality, and trends of southeast US aerosol: an integrated analysis of surface, aircraft, and
395 satellite observations with the GEOS-Chem chemical transport model, *Atmospheric Chem.
396 Phys.*, 15, 10411–10433, <https://doi.org/10.5194/acp-15-10411-2015>, 2015.

397 Lin, H., [Feng, X., Fu, T.-M., Tian, H., Ma, Y., Zhang, L., Jacob, D. J., Yantosca, R. M., Sulprizio,](#)
398 [M. P., Lundgren, E. W., Zhuang, J., Zhang, Q., Lu, X., Zhang, L., Shen, L., Guo, J., Eastham, S.](#)
399 [D., and Keller, C. A.: WRF-GC \(v1.0\): online coupling of WRF \(v3.9.1.1\) and GEOS-Chem](#)
400 [\(v12.2.1\) for regional atmospheric chemistry modeling – Part 1: Description of the one-way](#)
401 [model, Geosci. Model Dev., 13, 3241–3265, <https://doi.org/10.5194/gmd-13-3241-2020>, 2020.](#)

402 [Lin, H., Jacob, D. J., Lundgren, E. W., Sulprizio, M. P., Keller, C. A., Fritz, T. M., Eastham, S.](#)
403 [D., Emmons, L. K., Campbell, P. C., Baker, B., Saylor, R. D., and Montuoro, R.: Harmonized](#)
404 [Emissions Component \(HEMCO\) 3.0 as a versatile emissions component for atmospheric](#)
405 [models: application in the GEOS-Chem, NASA GEOS, WRF-GC, CESM2, NOAA GEFS-](#)
406 [Aerosol, and NOAA UFS models, Geosci. Model Dev., 14, 5487–5506,](#)
407 <https://doi.org/10.5194/gmd-14-5487-2021>, 2021.

408 Lin, J.-T. and McElroy, M. B.: Impacts of boundary layer mixing on pollutant vertical profiles in
409 the lower troposphere: Implications to satellite remote sensing, *Atmos. Environ.*, 44, 1726–1739,
410 <https://doi.org/10.1016/j.atmosenv.2010.02.009>, 2010.

411 [Lin, S.-J. and Rood, R. B.: Multidimensional flux-form semi-lagrangian transport schemes, *Mon.*](#)
412 [Weather Rev., 124, 2046–2070, \[0493\\(1996\\)124%3C2046:MFFSLT%3E2.0.CO;2, 1996.\]\(https://doi.org/10.1175/1520-
413 <a href=\)](#)

414 Liu, H., Jacob, D. J., Bey, I., and Yantosca, R. M.: Constraints from 210Pb and 7Be on wet
415 deposition and transport in a global three-dimensional chemical tracer model driven by
416 assimilated meteorological fields, *J. Geophys. Res. Atmospheres*, 106, 12109–12128,
417 <https://doi.org/10.1029/2000JD900839>, 2001.

418 Lu, X., Hong, J., Zhang, L., Cooper, O. R., Schultz, M. G., Xu, X., Wang, T., Gao, M., Zhao, Y.,
419 and Zhang, Y.: Severe surface ozone pollution in china: A global perspective, *Environ. Sci.*
420 *Technol. Lett.*, 5, 487–494, <https://doi.org/10.1021/acs.estlett.8b00366>, 2018.

421 [Lu, X., Zhang, L., Wu, T., Long, M. S., Wang, J., Jacob, D. J., Zhang, F., Zhang, J., Eastham, S.](#)
422 [D., Hu, L., Zhu, L., Liu, X., and Wei, M.: Development of the global atmospheric chemistry](#)
423 [general circulation model BCC-GEOS-Chem v1.0: model description and evaluation, *Geosci.*](#)
424 [Model Dev., 13, 3817–3838, <https://doi.org/10.5194/gmd-13-3817-2020>, 2020.](#)

425 Maasackers, J. D., McDuffie, E. E., Sulprizio, M. P., Chen, C., Schultz, M., Brunelle, L., Thrush,
426 R., Steller, J., Sherry, C., Jacob, D. J., Jeong, S., Irving, B., and Weitz, M.: A gridded inventory
427 of annual 2012–2018 U.S. anthropogenic methane emissions, *Environ. Sci. Technol.*, 57, 16276–
428 16288, <https://doi.org/10.1021/acs.est.3c05138>, 2023.

429 Martin, R. V., Eastham, S. D., Bindle, L., Lundgren, E. W., Clune, T. L., Keller, C. A., Downs,
430 W., Zhang, D., Lucchesi, R. A., Sulprizio, M. P., Yantosca, R. M., Li, Y., Estrada, L., Putman, W.
431 M., Auer, B. M., Trayanov, A. L., Pawson, S., and Jacob, D. J.: Improved advection, resolution,
432 performance, and community access in the new generation (version 13) of the high-performance
433 GEOS-Chem global atmospheric chemistry model (GCHP), *Geosci. Model Dev.*, 15, 8731–8748,
434 <https://doi.org/10.5194/gmd-15-8731-2022>, 2022.

435 Philip, S., Martin, R. V., and Keller, C. A.: Sensitivity of chemistry-transport model simulations
436 to the duration of chemical and transport operators: a case study with GEOS-Chem v10-01,
437 *Geosci. Model Dev.*, 9, 1683–1695, <https://doi.org/10.5194/gmd-9-1683-2016>, 2016.

438 [Stanevich, I., Jones, D. B. A., Strong, K., Parker, R. J., Boesch, H., Wunch, D., Notholt, J., Petri,](#)
439 [C., Warneke, T., Sussmann, R., Schneider, M., Hase, F., Kivi, R., Deutscher, N. M., Velazco, V.](#)
440 [A., Walker, K. A., and Deng, F.: Characterizing model errors in chemical transport modeling of](#)
441 [methane: impact of model resolution in versions v9-02 of GEOS-Chem and v35j of its adjoint](#)
442 [model, *Geosci. Model Dev.*, 13, 3839–3862, <https://doi.org/10.5194/gmd-13-3839-2020>, 2020.](#)

443 US Census Bureau, TIGER/Line Shapefile, 2017, 2010 nation, U.S., 2010 Census Urban Area
444 National. [https://catalog.data.gov/dataset/tiger-line-shapefile-2017-2010-nation-u-s-2010-census-](https://catalog.data.gov/dataset/tiger-line-shapefile-2017-2010-nation-u-s-2010-census-urban-area-national)
445 [urban-area-national](https://catalog.data.gov/dataset/tiger-line-shapefile-2017-2010-nation-u-s-2010-census-urban-area-national). Deposited 1 August 2019.

446 Varon, D. J., Jacob, D. J., Sulprizio, M., Estrada, L. A., Downs, W. B., Shen, L., Hancock, S. E.,
447 Nesser, H., Qu, Z., Penn, E., Chen, Z., Lu, X., Lorente, A., Tewari, A., and Randles, C. A.:
448 Integrated Methane Inversion (IMI 1.0): a user-friendly, cloud-based facility for inferring high-
449 resolution methane emissions from TROPOMI satellite observations, *Geosci. Model Dev.*, 15,
450 5787–5805, <https://doi.org/10.5194/gmd-15-5787-2022>, 2022.

451 Wang, X., Jacob, D. J., Downs, W., Zhai, S., Zhu, L., Shah, V., Holmes, C. D., Sherwen, T.,
452 Alexander, B., Evans, M. J., Eastham, S. D., Neuman, J. A., Veres, P. R., Koenig, T. K.,
453 Volkamer, R., Huey, L. G., Bannan, T. J., Percival, C. J., Lee, B. H., and Thornton, J. A.: Global
454 tropospheric halogen (Cl, Br, I) chemistry and its impact on oxidants, *Atmospheric Chem. Phys.*,
455 21, 13973–13996, <https://doi.org/10.5194/acp-21-13973-2021>, 2021.

456 Wang, X., Jacob, D. J., Nesser, H., Balasus, N., Estrada, L. A., Sulprizio, M. P., Cusworth, D. H.,
457 Scarpelli, T. R., Chen, Z., East, J. D., and Varon, D. J.: Quantifying urban and landfill methane
458 emissions in the United States using TROPOMI satellite data, *Sci. Adv.*, 12, eadz9308,
459 <https://doi.org/10.1126/sciadv.adz9308>, 2026.

460 Wang, Y. X., McElroy, M. B., Jacob, D. J., and Yantosca, R. M.: A nested grid formulation for
461 chemical transport over Asia: Applications to CO, *J. Geophys. Res. Atmospheres*, 109,
462 <https://doi.org/10.1029/2004JD005237>, 2004.

463 Wecht, K. J., Jacob, D. J., Frankenberg, C., Jiang, Z., and Blake, D. R.: Mapping of North
464 American methane emissions with high spatial resolution by inversion of SCIAMACHY satellite
465 data, *J. Geophys. Res. Atmospheres*, 119, 7741–7756, <https://doi.org/10.1002/2014JD021551>,
466 2014.

467 Yu, K., Keller, C. A., Jacob, D. J., Molod, A. M., Eastham, S. D., and Long, M. S.: Errors and
468 improvements in the use of archived meteorological data for chemical transport modeling: an
469 analysis using GEOS-Chem v11-01 driven by GEOS-5 meteorology, *Geosci. Model Dev.*, 11,
470 305–319, <https://doi.org/10.5194/gmd-11-305-2018>, 2018.

471 Zhai, S., Jacob, D. J., Wang, X., Shen, L., Li, K., Zhang, Y., Gui, K., Zhao, T., and Liao, H.: Fine
472 particulate matter (PM_{2.5}) trends in China, 2013–2018: separating contributions from

473 anthropogenic emissions and meteorology, *Atmospheric Chem. Phys.*, 19, 11031–11041,
474 <https://doi.org/10.5194/acp-19-11031-2019>, 2019.

475 Zhai, S., Jacob, D. J., Brewer, J. F., Li, K., Moch, J. M., Kim, J., Lee, S., Lim, H., Lee, H. C.,
476 Kuk, S. K., Park, R. J., Jeong, J. I., Wang, X., Liu, P., Luo, G., Yu, F., Meng, J., Martin, R. V.,
477 Travis, K. R., Hair, J. W., Anderson, B. E., Dibb, J. E., Jimenez, J. L., Campuzano-Jost, P., Nault,
478 B. A., Woo, J.-H., Kim, Y., Zhang, Q., and Liao, H.: Relating geostationary satellite
479 measurements of aerosol optical depth (AOD) over East Asia to fine particulate matter (PM_{2.5}):
480 insights from the KORUS-AQ aircraft campaign and GEOS-Chem model simulations,
481 *Atmospheric Chem. Phys.*, 21, 16775–16791, <https://doi.org/10.5194/acp-21-16775-2021>, 2021.

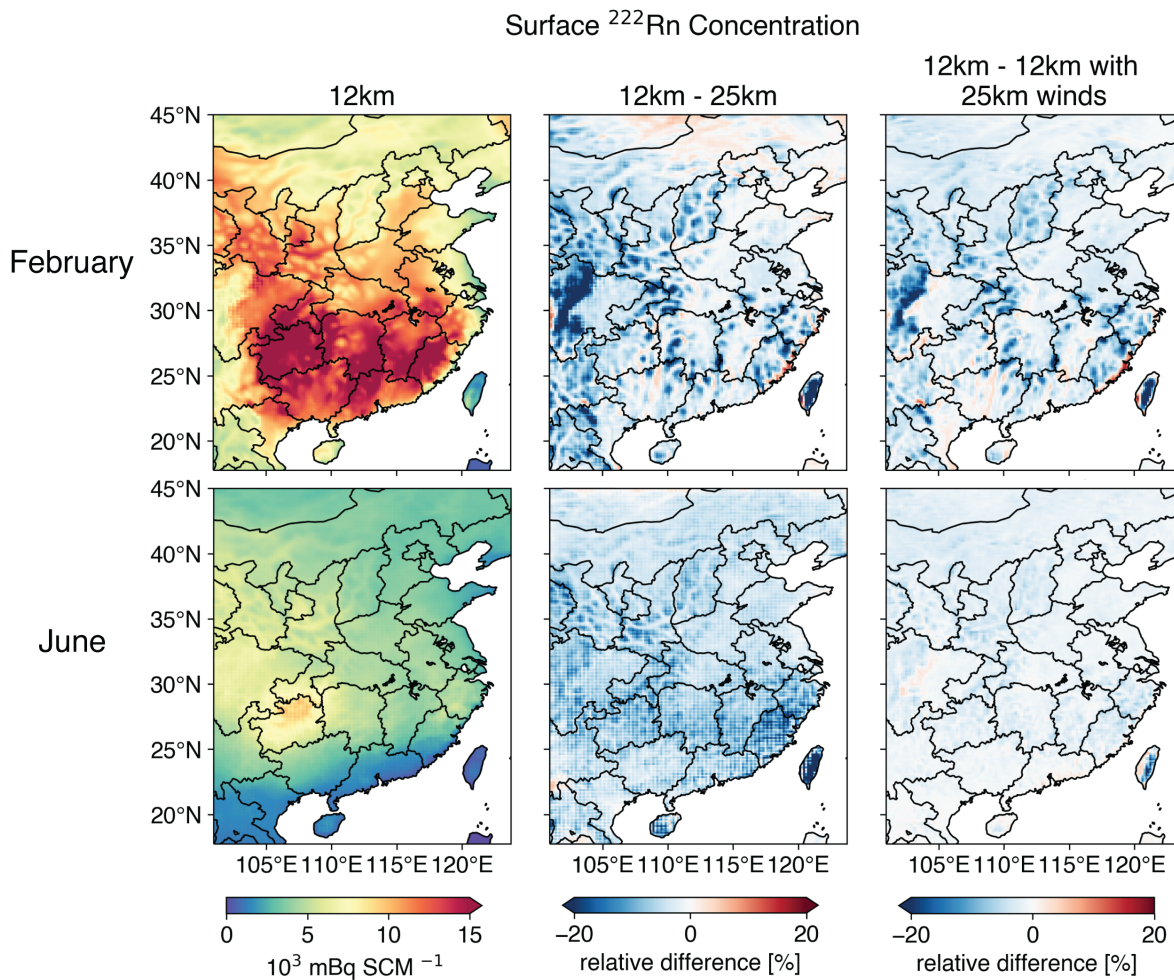
482 Zhang, [B.](#), [Liu, H.](#), [Crawford, J. H.](#), [Chen, G.](#), [Fairlie, T. D.](#), [Chambers, S.](#), [Kang, C.-H.](#),
483 [Williams, A. G.](#), [Zhang, K.](#), [Considine, D. B.](#), [Sulprizio, M. P.](#), and [Yantosca, R. M.](#): [Simulation](#)
484 [of radon-222 with the GEOS-Chem global model: emissions, seasonality, and convective](#)
485 [transport](#), *Atmospheric Chem. Phys.*, 21, 1861–1887, <https://doi.org/10.5194/acp-21-1861-2021>,
486 [2021](#).

487 [Zhang, L.](#), Liu, L., Zhao, Y., Gong, S., Zhang, X., Henze, D. K., Capps, S. L., Fu, T.-M., Zhang,
488 Q., and Wang, Y.: Source attribution of particulate matter pollution over North China with the
489 adjoint method, *Environ. Res. Lett.*, 10, 084011, <https://doi.org/10.1088/1748-9326/10/8/084011>,
490 2015.

491 Zheng, B., Tong, D., Li, M., Liu, F., Hong, C., Geng, G., Li, H., Li, X., Peng, L., Qi, J., Yan, L.,
492 Zhang, Y., Zhao, H., Zheng, Y., He, K., and Zhang, Q.: Trends in China's anthropogenic
493 emissions since 2010 as the consequence of clean air actions, *Atmospheric Chem. Phys.*, 18,
494 14095–14111, <https://doi.org/10.5194/acp-18-14095-2018>, 2018.

495 Zhuang, J., Jacob, D. J., Gaya, J. F., Yantosca, R. M., Lundgren, E. W., Sulprizio, M. P., and
496 Eastham, S. D.: Enabling Immediate Access to Earth Science Models through Cloud Computing:
497 Application to the GEOS-Chem Model, *Bull. Am. Meteorol. Soc.*, 100, 1943–1960,
498 <https://doi.org/10.1175/BAMS-D-18-0243.1>, 2019.

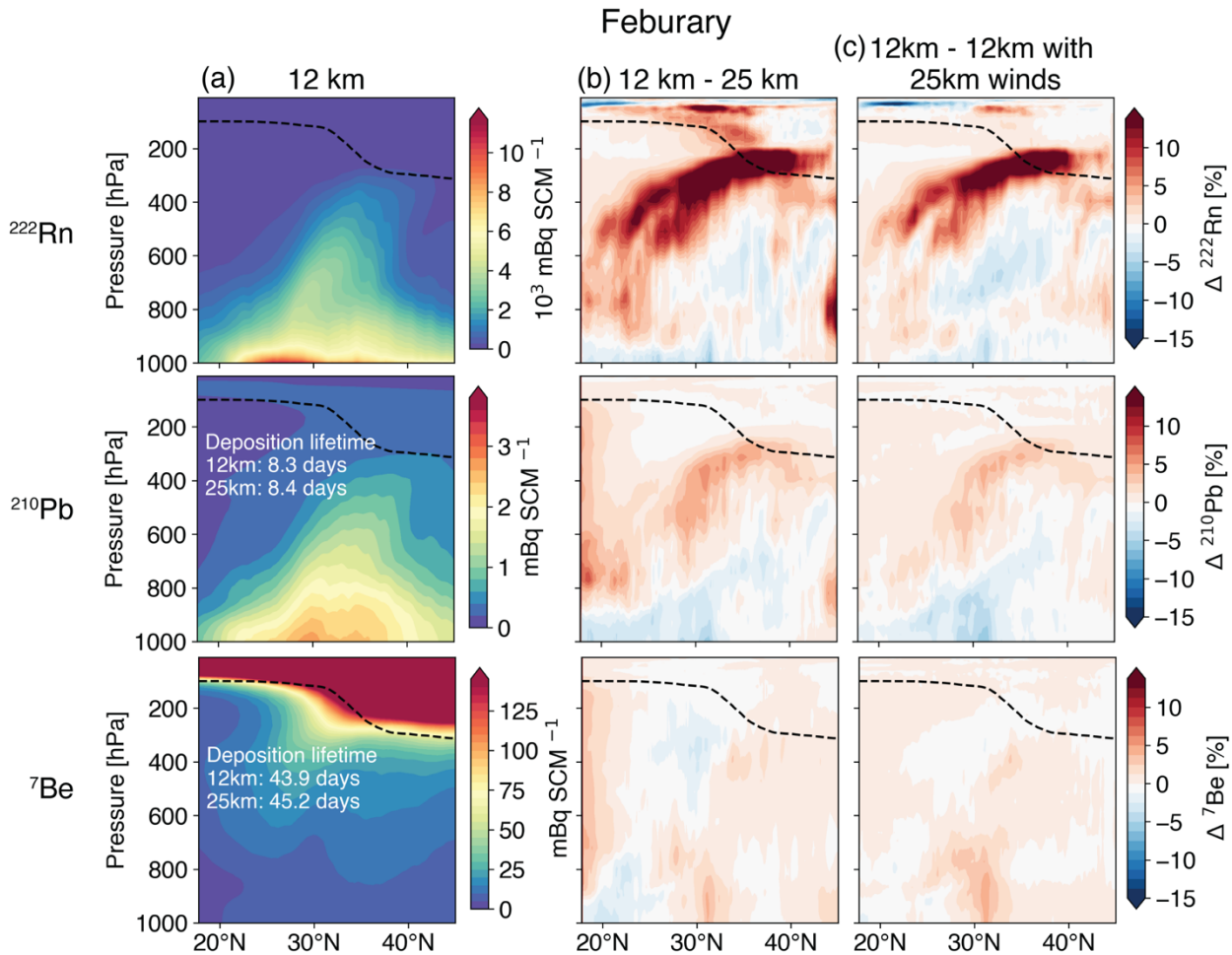
499



501 **Figure 1.** Monthly mean surface ^{222}Rn mixing ratios (mBq SCM^{-1}) simulated over eastern China
 502 in February and June 2022. Columns from left to right show the concentrations simulated by
 503 GEOS-Chem at 12-km resolution, ~~and~~the relative differences with a simulation at 25-km
 504 resolution, ~~for February and June 2022.~~ and the relative differences between two 12-km
 505 simulations driven by the 12-km and 25-km GEOS-FP advection archives, respectively. SCM is
 506 a standard cubic meter of air at 0 °C (273.15 K) and 1 atm (1013.25 hPa).

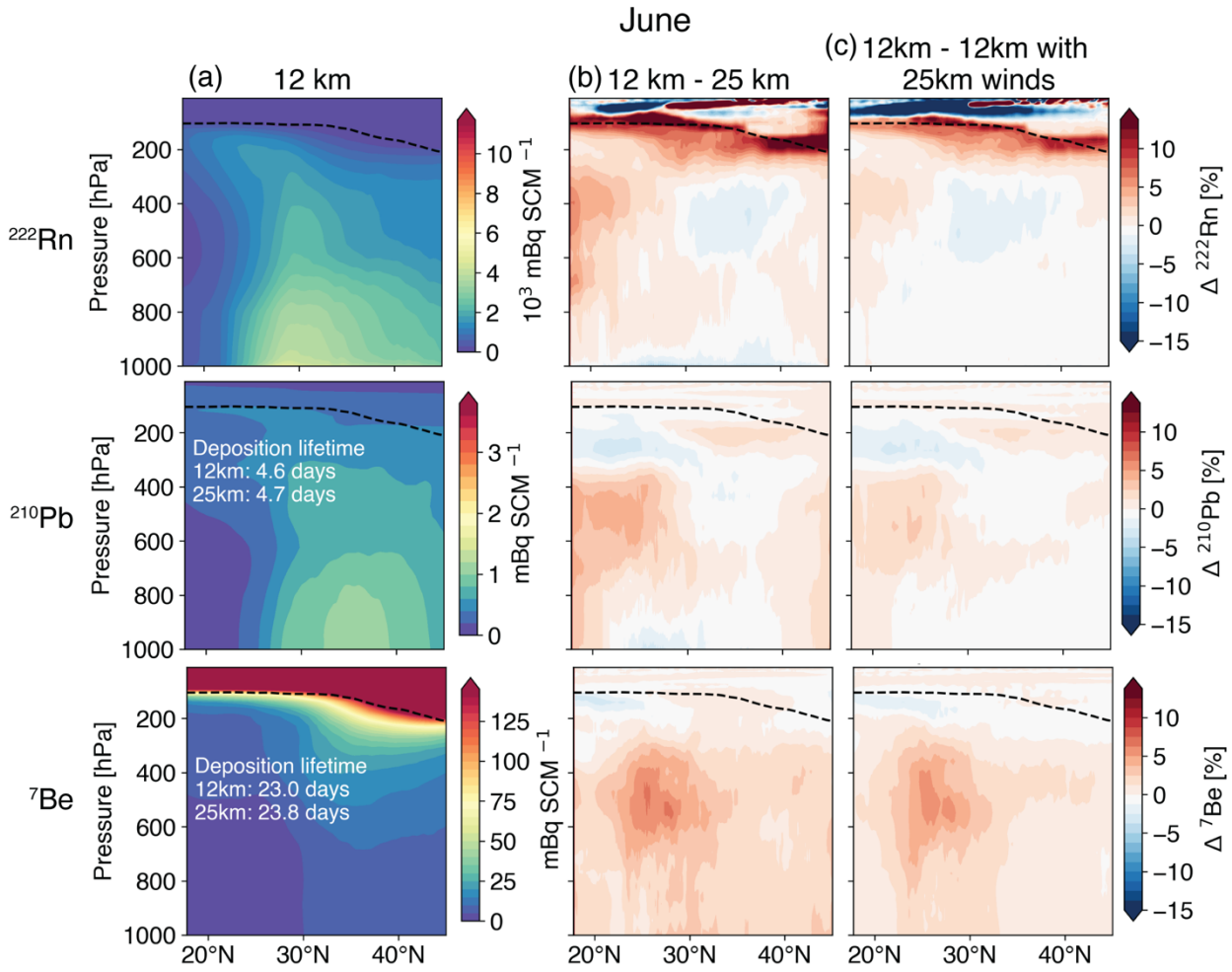
507

508



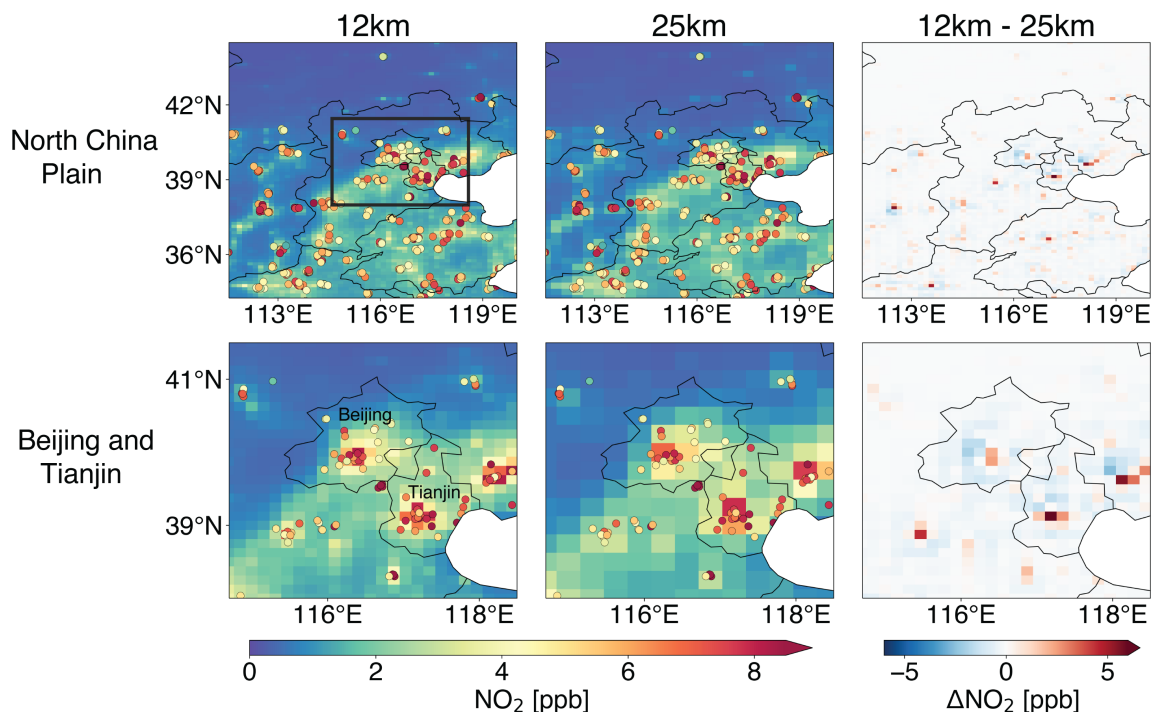
510 **Figure 2.** Zonally averaged latitude-pressure monthly mean mixing ratios of ^{222}Rn , ^{210}Pb , and
 511 ^{7}Be simulated by GEOS-Chem for February 2022 over the eastern China domain of Figure 1 at
 512 12-km resolution; (left column), the relative differences with a 25-km simulation (middle
 513 column) and relative differences with a 25-km simulation, for February and June 2022 over
 514 China (domain of Figure 1); 12-km simulation driven by the 25-km advection archive (right
 515 column) Lifetimes of tropospheric ^{210}Pb and ^{7}Be against deposition are inset. The dashed black
 516 lines indicate the tropopause.

517



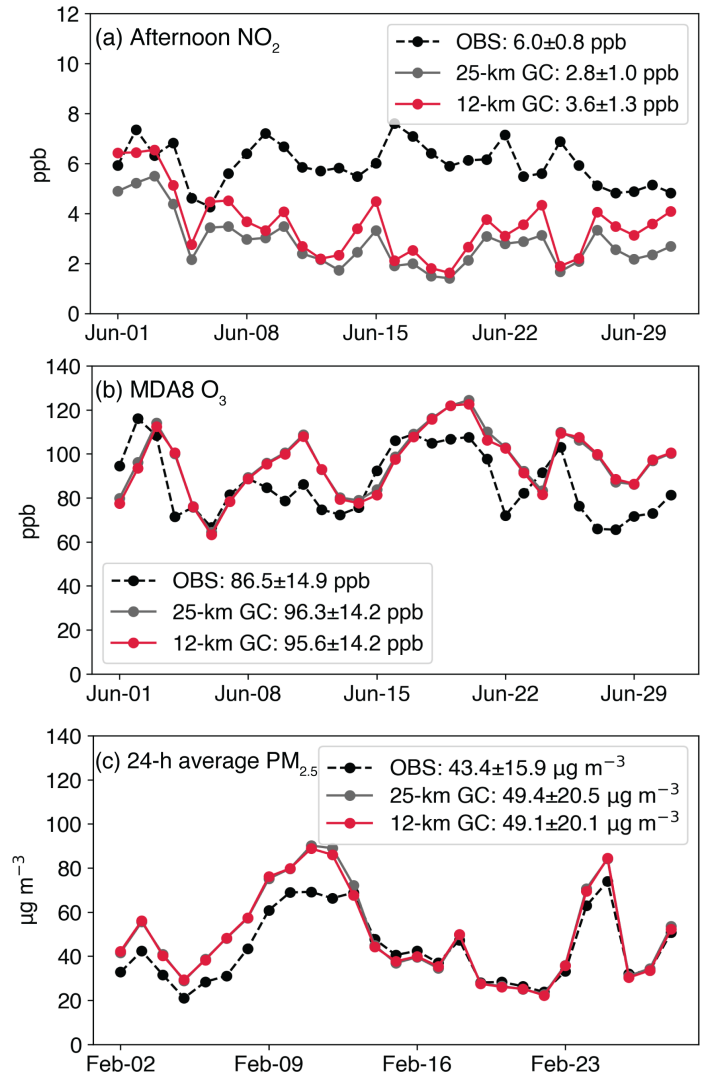
519 **Figure 3.** [Same as Figure 2 but for June 2022.](#)

522
523
524
525



526 **Figure 4.** Afternoon (13–18 local time) monthly mean surface NO₂ concentrations in June 2022
527 simulated by GEOS-Chem at 12-km and 25-km resolution, for the North China Plain (NCP) and
528 for Beijing and Tianjin (box in top left panel). Circles show CNEMC network observations.

529



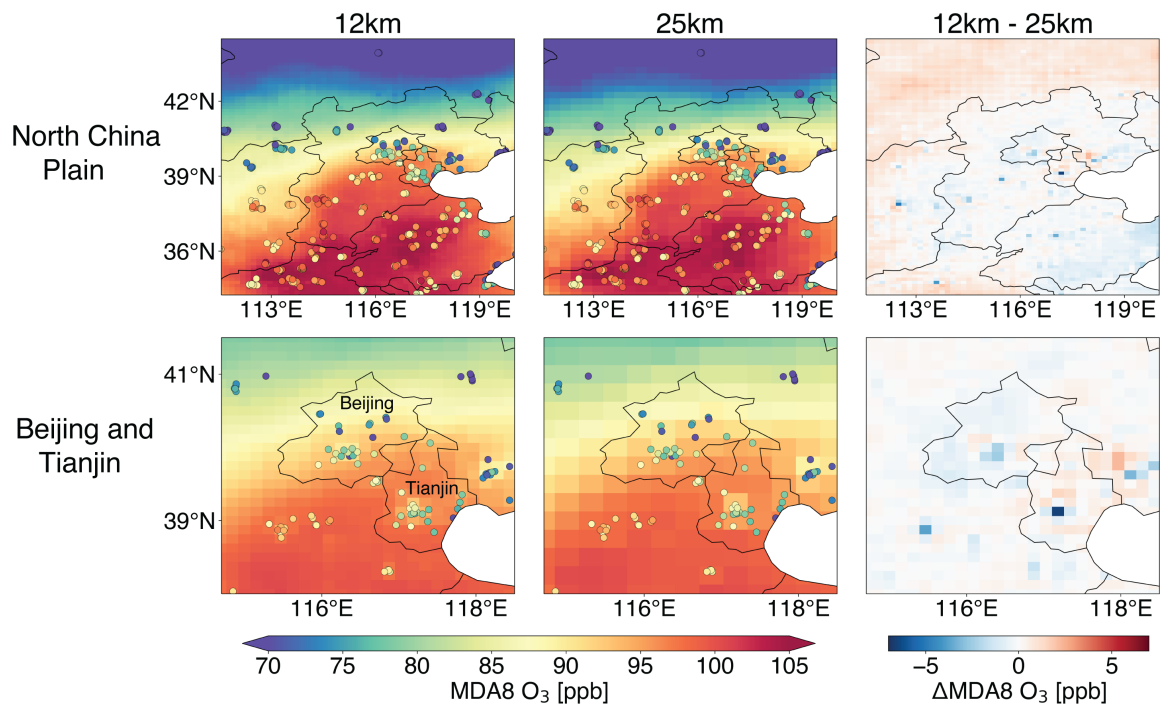
530

531

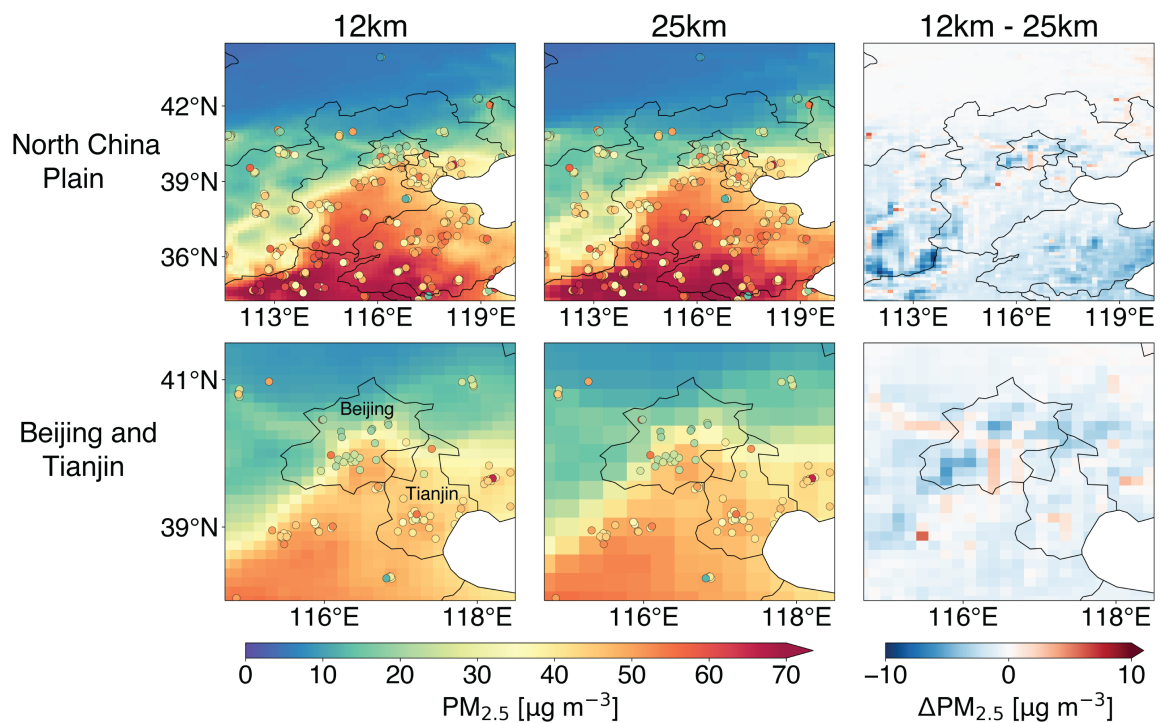
532 **Figure 45.** Daily time series of surface concentrations in the North China Plain (NCP): (a)
 533 afternoon (13–18 local time) NO_2 in June 2022, (b) maximum daily 8-h average (MDA8) ozone
 534 in June 2022, and (c) 24-h average $\text{PM}_{2.5}$ in February 2022. Observations at China National
 535 Environmental Monitoring Center (CNEMC) sites, shown as circles in Figure 34 and averaged
 536 over the NCP domain, are compared to GEOS-Chem simulations at 12- and 25-km resolution for
 537 the same sites. Monthly mean values and standard deviations across all domain sites are shown
 538 inset.

539

540

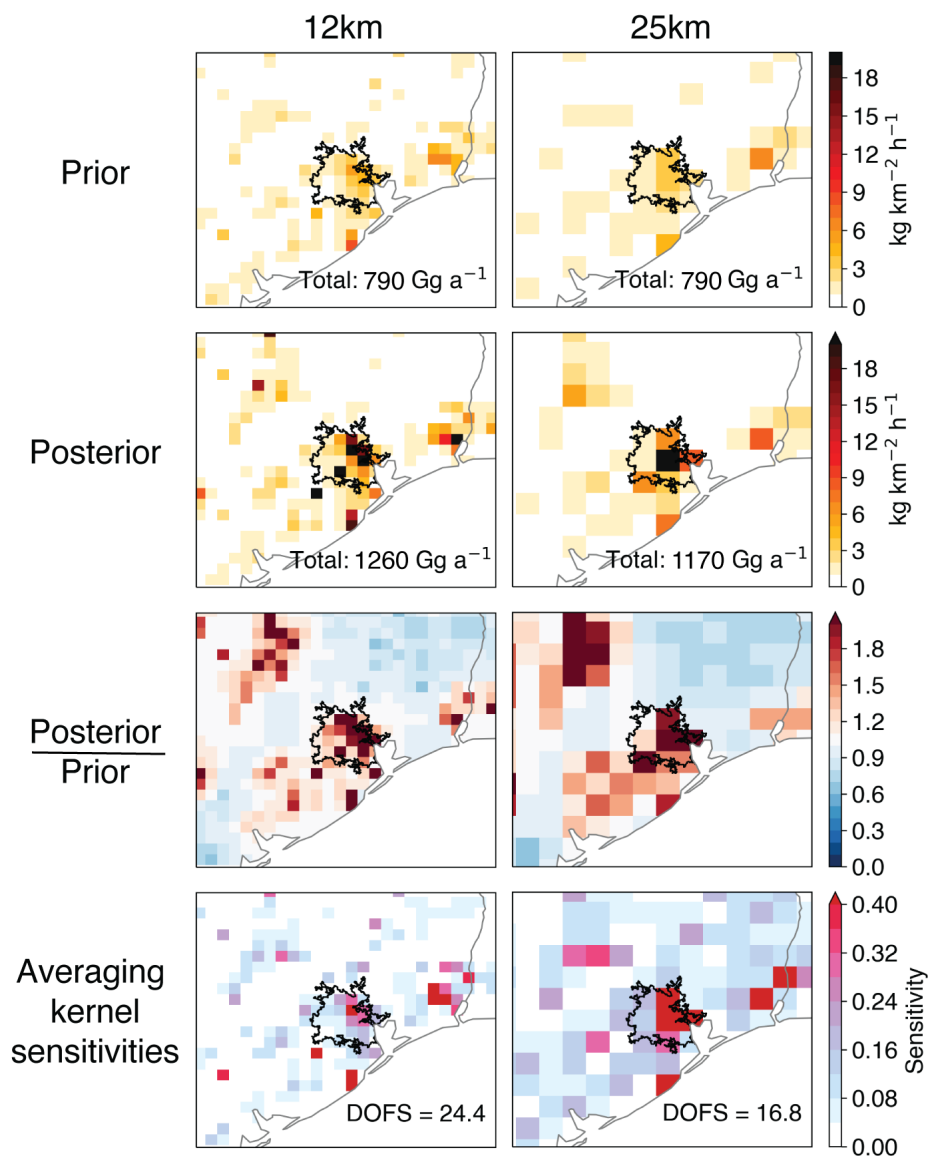


541 **Figure 56.** Same as Figure 34 but for surface MDA8 ozone concentrations in June 2022.



542
 543 **Figure 6-Figure 7.** Same as Figure 34 but for surface 24-h average PM_{2.5} concentrations in
 544 February 2022.

545



547

548 **Figure 78.** Methane emissions in the Houston area of eastern Texas ($3^\circ \times 4^\circ$ domain) inferred
 549 from TROPOMI satellite observations using the Integrated Methane Inversion (IMI) at 12- and
 550 25-km resolution. Panels from top to bottom are prior emissions from bottom-up inventories;
 551 posterior emissions from the inversion; ratio of posterior to prior emissions; and averaging kernel
 552 sensitivities that quantify the sensitivity of the posterior estimates to the true state. The Houston
 553 urban boundary (US Census Bureau, 2017) is delineated in black. Emission totals over the whole
 554 $3^\circ \times 4^\circ$ domain are shown inset in the top two rows. The sum of area-weighted averaging kernel
 555 sensitivities for the whole domain defines the Degrees of Freedom for Signal (DOFS) inset in the
 556 bottom panels.